NOVEL MAGNETIC-FIELD-INDUCED MINIGAP AND TRANSPORT IN COUPLED DOUBLE QUANTUM WELLS

S. K. LYO, J. A. SIMMONS, N. E. HARFF, AND J. F. KLEM
Sandia National Laboratories, Albuquerque, NM 87185, USA

ABSTRACT

A review is given of recent theoretical and experimental work on in-plane electron transport in strongly coupled double quantum wells (QWs) in the presence of an in-plane magnetic field $\mathbf{B}_{||} \parallel \mathbf{x}$. This system displays unusual electronic and transport properties arising from a partial minigap (~ a few meV) formed in the transverse in-plane direction $\mathbf{k}_y \perp \mathbf{B}_{||}$ in $\mathbf{k}$-space due to the anticrossing of the two QW dispersion curves displaced relative to each other by $\Delta k_y \propto B_{||}$. Sweeping $B_{||}$ moves the minigap through the Fermi level (μ), deforming the Fermi surface from a two-component surface (with one orbit inside the other) to a single-orbit surface, and then back to a two-separated-orbit structure, accordingly as μ lies above, inside, and below the gap, respectively. We show that the density of states develops a sharp van Hove singularity at the lower gap edge, while transport properties such as the in-plane conductance and the cyclotron mass show sharp $B_{||}$-dependent structures as μ passes through the gap edges.

1. Introduction

Currently, double quantum well (DQW) structures are receiving increasing attention for new physical phenomena and possible 2D-2D (two-dimensional) tunneling devices. These systems consist of double layers of 2D degenerate electron gases (2DEGs) separated by a thin barrier as shown in Fig. 1. In DQW structures, the inter-quantum-well separation and the degree of tunneling provide a controllable extra degree of freedom compared to single-QW structures. New phenomena arise from direct or phonon-mediated inter-QW electron-electron interaction effects (i.e., Coulomb-drag effect) [1] as well as from the combined effect of tunneling and electron-electron interactions (i.e., Coulomb-barrier effect) [2]. In this paper, we review our recent theoretical and experimental work on another class of phenomenon arising solely from tunneling effects in strongly-coupled DQWs subject to an in-plane magnetic field $\mathbf{B}_{||} \parallel \mathbf{x}$. This system has been shown to have many interesting electronic and transport properties [3-9]. These $B_{||}$-dependent properties include sharp structures in the density of states (DOS), Fermi surfaces that vary continuously with $B_{||}$, the in-plane conductance, and the cyclotron mass. These unusual features are caused by a partial minigap (~ a few meV) created in the transverse in-plane direction $\mathbf{k}_y$ ($\perp \mathbf{B}_{||}$) by the anticrossing of the two energy-dispersion parabolas of the QWs. These parabolas are displaced relative to each other in $\mathbf{k}$-space by $\Delta k_y = d / \ell^2$ where $\ell = (\hbar c / eB_{||})^{1/2}$ is the classical magnetic length and d is the center-to-center distance between the two QWs. Sweeping $B_{||}$ moves the minigap through the Fermi level (μ), deforming the Fermi surface from a two-component surface (with one orbit inside the other), to a single-

DISCLAIMER

Portions of this document may be illegible in electronic image products. Images are produced from the best available original document.

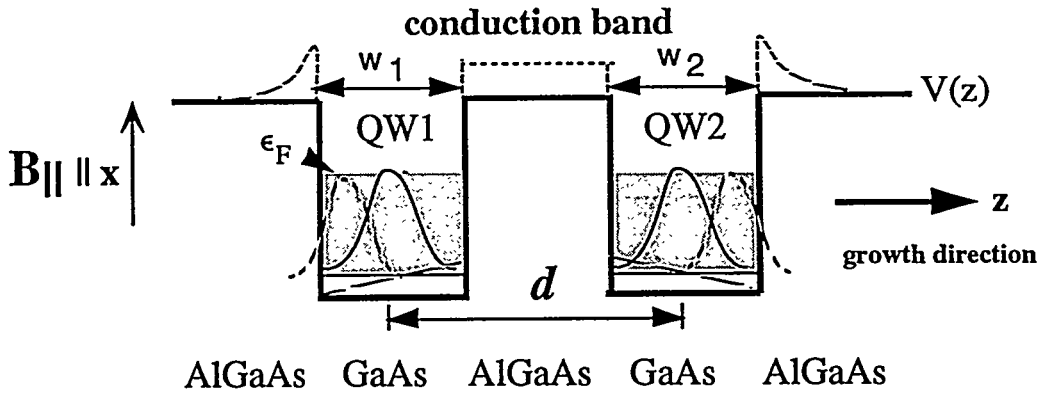

FIG. 1. GaAs/AlGaAs double quantum wells with 2DEGs shown by the shaded area. The confinement wave functions move away from each other due to band-bending as shown by the dashed curves, increasing the effective distance between the wells. The horizontal bars beneath the 2DEGs signify the sublevels.

orbit surface, and then finally back to a two-separated-orbit structure as μ lies above, inside, and below the gap, respectively. We show that 1) the density of states develops a sharp van Hove singularity at the saddle point formed at the lower gap edge, 2) the in-plane conductance exhibits maximum and minimum when μ lies at the upper and lower gap edges, respectively, and 3) the cyclotron mass undergoes abrupt $B_{||}$-dependent changes as μ passes through the gap edges.

The organization of the paper is as follows. In Sec. 2, we introduce the Hamiltonian and obtain the $B_{||}$-dependent electronic structure including the Fermi surface and the chemical potential. The in-plane magneto-conductance and cyclotron mass are discussed in Secs. 3 and 4, respectively. Brief concluding remarks are given in Sec. 5.

2. Hamiltonian and Electronic Structure

In the presence of an in-plane magnetic field, the Hamiltonian is given by

$$H = \frac{p_z^2}{2m^*} + \frac{\hbar^2}{2m^*}(k_y - \frac{z}{\ell^2})^2 + V(z), \tag{1}$$

where $p_z = -i\hbar\partial/\partial z$ and, for simplicity, the same isotropic effective mass m^* is used in the QW's and the barriers, although m^* is somewhat larger in the AlGaAs barriers. However, this is a good approximation because the confinement wave functions have negligible penetration into the barrier regions owing to large barrier heights. The kinetic energy $\varepsilon(k_x) = (\hbar k_x)^2/2m^*$ in the direction of $\mathbf{B}_{||}$ is to be added to (1). Note that the 2D wave vector $\mathbf{k}$ is a good quantum number in $\mathbf{B}_{||}$. The confinement potential $V(z)$ is a superposition of the potentials $V_1(z)$ and $V_2(z)$ of QW1 and QW2. In the absence of band-bending, $V_1(z)$ and $V_2(z)$ are square-well potentials with well-widths w_1, w_2 respectively and depths V_o. We assume quasi-two-dimensional (i.e., w_1, $w_2 < \ell$) thin QW's where only the ground sublev-

els are populated. The latter are designated by horizontal bars in Fig. 1 beneath the 2DEGs denoted by the shaded area. While the Hamiltonian in (1) can, in general, be diagonalized numerically, we consider here only approximate, but accurate analytic solutions by including only the lowest two sublevels in narrow QW's. Using the field-free ground-sublevel eigenfunctions of the isolated single-QW's $\phi_1(z)$ and $\phi_2(z)$ as the basis functions with eigenvalues ε_1 and ε_2, we find [3]

$$\varepsilon_{\pm}(k_y)=\frac{1}{2(1-S^2)}\left(H_{11}+H_{22}-2SH_{12}\pm\sqrt{D}\right), \tag{2a}$$

and

$$D=(H_{11}-H_{22})^2(1-S^2)+[(H_{11}+H_{22})S-2H_{12}]^2, \tag{2b}$$

where $S = <\phi_1|\phi_2>$. The matrix elements H_{nm} are given by

$$H_{nm}=\varepsilon_m<\phi_n|\phi_m>+<\phi_n|V_{m'}(z)|\phi_m>+<\phi_n|V_B(z)|\phi_m> \quad (n,m=1,2) \tag{2c}$$

where the prime on the subscript m' signifies that $1' = 2$, $2' = 1$ and $V_B(z)$ is the second term in (1). For symmetric DQWs, (2a) is simplified, to the lowest order in the overlap factor $S_{12} = <\phi_1(z)|\phi_2(z)>$, as [9]

$$\varepsilon_{\pm}(k_y)=\varepsilon(k_y)+\frac{d_1^2+(\Delta z_1)^2}{\ell^2}\varepsilon_\ell\pm\left(4\varepsilon_\ell\varepsilon(k_y)d_1^2/\ell^2+(\frac{E_g}{2})^2\right)^{1/2}+\frac{E_g}{2}, \tag{3}$$

where $\varepsilon(k_y) = (\hbar k_y)^2/2m^*$, $\varepsilon_\ell = (\hbar\ell^{-1})^2/2m^*$, $d_n = |<z_n>|$, and $d_1 = d_2$. Here $<z_n> = <\phi_n(z)|z|\phi_n(z)>$ is the expectation value of z with respect to the wave function $\phi_n(z)$ and $(\Delta z_n)^2 = <\phi_n(z)|(z - <z_n>)^2|\phi_n(z)>$ is the mean square deviation of z arising from finite widths of the QWs. In (3), use is made of $\Delta z_1 = \Delta z_2$. The minigap is given by

$$E_g = 2|S_{12}<\phi_1(z)|V_2(z)|\phi_1(z)> - <\phi_1(z)|V_1(z)|\phi_2(z)>| \tag{4}$$

and is independent of $B_{||}$. The last term in (3) is added for convenience so that the lower branch energy $\varepsilon_-(k_y)$ vanishes at $k_y = 0$ in zero field.

As discussed in Sec. 1, the basic effect of $B_{||}$ is to displace the origins of the transverse crystal momenta k_y in the two QWs away from each other by $\Delta k_y = d/\ell^2$ where $d = d_1 + d_2$. As a result, the two energy-dispersion parabolas anticross in the presence of tunneling, yielding upper and lower branches in (2) and (3). A similar anticrossing of dispersion curves, although of different origin, is known to occur without magnetic fields in a vicinal surface such as the (911) surface of a Si-inversion layer and was studied extensively many years ago [10].

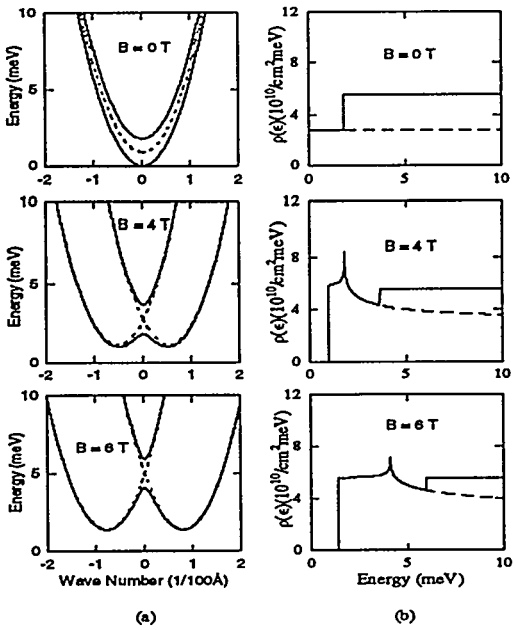

FIG. 2. (a) Energy dispersion curves of a symmetric DQW structure with (solid curves) and without (dashed curves) tunneling. (b) The DOS from the lower branch (dashed curves) and both branches (solid curves).

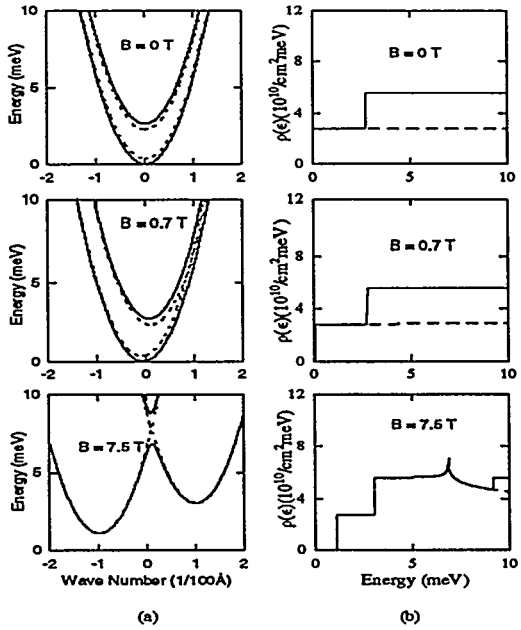

FIG. 3. (a) Energy dispersion curves of an asymmetric DQW structure with (solid curves) and without (dashed curves) tunneling. (b) The DOS from the lower (dashed curves) and both branches (solid curves).

The upper and lower branches of the eigenvalues $\varepsilon_{\pm}(k_y)$ are shown in Fig. 2(a) for several $B_{||}$'s for a symmetric GaAs/$Al_{0.3}Ga_{0.7}As$ DQW sample with $d = 175$ Å, $w_1 = w_2 = 150$ Å, a zero-field effective mass of $m^* = 0.067m_0$ (m_0 is the free-electron mass), and $V_0 = 280$ meV. Band bending has been neglected here, and will be discussed later in terms of the Hartree approximation. The sample has a total combined 2D density $N = 3\times10^{11}$ cm^{-2}. The dashed parabolas are the energy dispersion curves for uncoupled QW's, namely QW1 (left side) and QW2 (right side) alone. The two parabolas coincide at $B_{||} = 0$. As a result of tunneling, the parabolas anticross, forming a minigap, and separate into the upper and lower branches shown in solid curves. At low $B_{||}$'s, the bottoms of the parabolas rise very slowly as $\propto B_{||}^2\langle(z - \langle z\rangle)^2\rangle$. Here the angular brackets denote the expectation value. At higher $B_{||}$'s, the lower edge of the minigap lies at the local maximum of the lower branch and is a saddle point in **k**-space. The saddle point begins to appear at a high $B_{||}$ (i.e., about 4 T in Fig. 2(a)) when the energy separation of the crossing point from the bottom of the dashed parabolas in Fig. 2(a) is large enough to overcome the energy repulsion between the two branches. The dispersion near the saddle point of the lower branch is of the form: $\epsilon(k_x,k_y) = \epsilon_0 + (\hbar k_x)^2/2m^* - (\hbar k_y)^2/2m'$ where m' (> 0) is determined from the curvature at the saddle point and ϵ_0 is the energy at the saddle point. This type of energy dispersion (i.e., with a negative sign for the last term of $\epsilon(k_x,k_y)$) yields a weakly divergent Van Hove singularity for the DOS of the form $\rho(\epsilon) \propto -\ell n|\epsilon - \epsilon_0|$. The DOS is shown in Fig. 2(b) for several $B_{||}$'s. The singularity is clearly seen there and moves up with $B_{||}$ in accordance

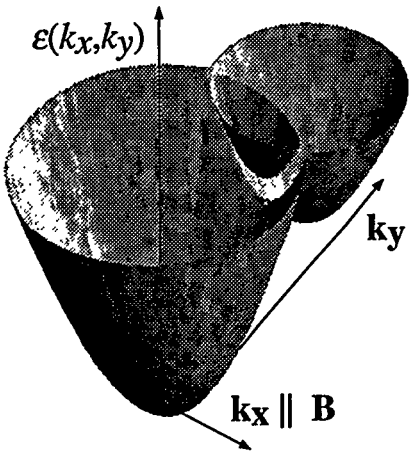

FIG. 4. Energy dispersion of the asymmetric DQW structure cited in Fig. 3. The Fermi surface is on the top equi-energy cross sectional layer and consists of a large hour-glass like orbit with an inner lens orbit at low fields.

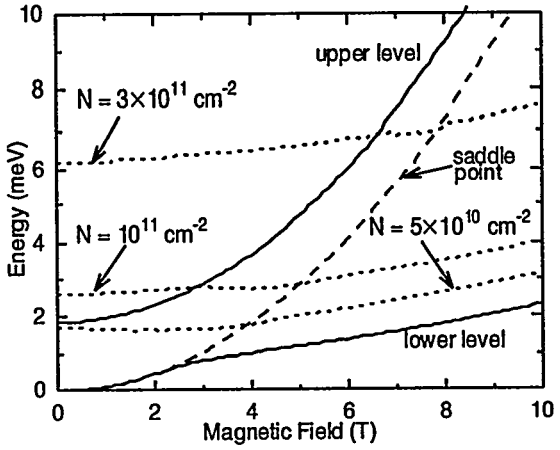

FIG. 5. Bottoms of the lower and upper branches (solid curves), saddle points (long-dashed curve) and chemical potentials (short-dashed curves) as a function of B.

with the $B_{||}$-dependent behavior of the saddle point shown in Fig. 2(a). This divergence is rounded [7] in the presence of damping of the levels.

For asymmetric DQWs, there are two different types of crossing (i.e., type I and type II) of the parabolas depending on the magnitude of $B_{||}$. In the type I crossing, $B_{||}$ is low so that the bottom of the upper parabola is inside the lower parabola and therefore the slopes of the tangents to the parabolas at the crossing point have the same sign. In this case, the anticrossing distorts the energy dispersion curves without opening a minigap. In contrast, in the type II crossing, $B_{||}$ is high so that the bottom of the upper parabola is outside the lower parabola and therefore the slopes have opposite signs, creating a minigap. These properties are demonstrated in Fig. 3(a) at two different $B_{||}$'s, namely at 0.7 and 7.5 T for an asymmetric DQW structure with d = 175 Å, $w_1 = w_2$ = 150 Å, V_1 = 280 meV, and V_2 = 278 meV. The DOS singularity appears only in the 7.5-T figure but not in the 0.7-T figure. In this case, the zero-$B_{||}$ splitting between the upper and lower branches in Fig. 3(a) is mainly due to different well depths, in contrast to Fig. 2.

The energy-dispersion surface of the cited asymmetric DQW structure is shown in Fig. 4. The top equi-energy cross section is a two-component Fermi surface which consists of a large hour-glass orbit with an inner lens-orbit. The shape of the Fermi surface varies continuously with $B_{||}$ as anticipated from the $B_{||}$-dependences of the energy dispersion curves shown in Figs. 2 and 3. In Fig. 5, the energies of the bottoms of both branches, as well as the lower gap edge (i.e., the saddle point), are shown in solid and long-dashed curves, respectively, as a function of $B_{||}$ for the symmetric DQWs. The chemical potential μ, plotted for three different electron densities in short-dashed curves, is insensitive to $B_{||}$ at low $B_{||}$'s and rises parallel to the bottom of the lower branch at high fields. The region

between the upper solid curve (i.e., the upper gap edge) and the long-dashed curve is the minigap. For the following discussions, it is important to notice that for high 2D carrier density (i.e., for $N = 10^{11}$ and 3×10^{11} cm^{-2}) the minigap passes through μ as $B_{||}$ is swept. For $N = 3\times10^{11}$ cm^{-2}, μ lies above, inside, and below the gap, respectively, as $B_{||}$ sweeps through the three regions $B_{||} < 6.6$ T, 6.6 T $< B_{||} <$ 7.85 T, and $B_{||} > 7.85$ T in Fig. 5. As can be guessed from Fig. 4 for the three concomitant equi-energy cross sections, the Fermi surface transforms successively from a two-component structure with an hour-glass orbit encircling a lens orbit similar to that shown in Fig. 4, to a one-component structure with only the outer hour-glass orbit, and then finally back to a two-component structure with two separated orbits. In the following sections, we examine the effect of the $B_{||}$-dependent electronic structure on the in-plane magnetotransport.

3. In-Plane Conductance

The longitudinal in-plane conductance is given in a relaxation-time approximation by [3]

$$G = \frac{e^2}{2\pi^2\hbar}\int \tau_{\mathbf{k}} \frac{(\mathbf{u}\bullet\mathbf{v}_{\mathbf{k}})^2}{v_{\mathbf{k}}} dk_{||}, \tag{5}$$

where $\mathbf{u}$ is a unit vector in the direction of the electric field, $\mathbf{v}_{\mathbf{k}} = \hbar^{-1}\nabla_{\mathbf{k}}\epsilon_{\mathbf{k}}$, $\epsilon_{\mathbf{k}} = \epsilon_x(k_x) + \epsilon_{\pm}(k_y)$, $v_{\mathbf{k}} = |\mathbf{v}_{\mathbf{k}}|$, $\tau_{\mathbf{k}}$ is the transport relaxation-time, and $\int dk_{||}$ is the linear integration along the orbit on the Fermi surface. We consider only elastic scattering at low temperatures. It is seen from (5) that the contribution from each portion of the Fermi surface is proportional to the velocity times the relaxation time. When μ is above the gap at low fields, the contribution to G arises from both the hour-glass orbit and the lens orbit in Fig. 4. However, the lens orbit contributes little to the current because 1) the electrons in the lens orbit move very slowly owing to the fact that they have small k values and 2) the number of states in the lens orbit is much smaller than in the hour-glass orbit. On the contrary, the lens orbit reduces $\tau_{\mathbf{k}}$ and therefore G in (5) by providing states into which the electrons in the hour-glass orbit are scattered rapidly at low fields. As $B_{||}$ is increased, the Fermi level μ passes through the upper gap edge depopulating the lens orbit. In this case, the electrons in the hour-glass orbit cannot be scattered into the upper branch elastically. As a result, $\tau_{\mathbf{k}}$ as well as G increases significantly. This behavior is shown by the solid curve (i.e., $\Gamma_0 = 0$ meV) in Fig. 6, where we plot G calculated from (5) for the symmetric DQW sample with $d = 175$ Å by approximating $\tau_{\mathbf{k}} \propto \rho(\varepsilon)^{-1}$. Here $\rho(\varepsilon)$ is the DOS. The abrupt increase in G in Fig. 6 occurs at the $B_{||}$ where μ crosses the upper solid curve for $N = 3\times10^{11}$ cm^{-2} in Fig. 5. On the other hand, when μ lies on the saddle point (i.e., at $B_{||} = 7.85$ T in Fig. 5), G vanishes because $\tau_{\mathbf{k}} \propto \rho(\varepsilon)^{-1} = 0$ due to the divergence of the DOS for $\Gamma_0 = 0$ meV as shown in Fig. 6. The effect of band bending is taken into account, by a self-consistent Hartree approximation. The new potential moves the confinement wave functions toward the external interfaces as illustrated by the dashed curves in Fig. 1, resulting in the increase of the effective well-to-well distance to $d = 2|\langle z_1\rangle| = 200$ Å. Since $B_{||}$ enters the Hamiltonian approximately as $d/\ell^2 \propto B_{||}d$, the $B_{||}$ positions of the maximum and minimum of G in Fig.

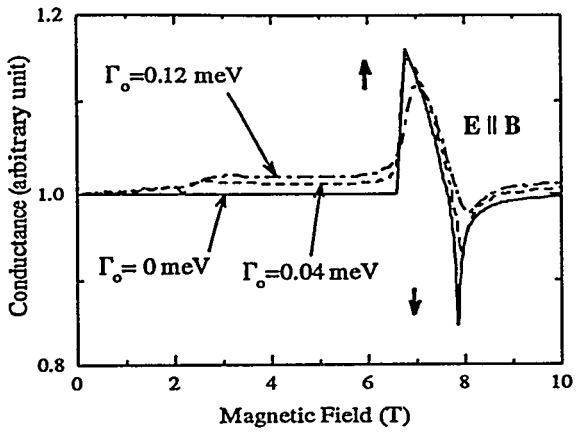

FIG. 6. Calculated in-plane conductance as a function of $B_{||}$ for the symmetric DQWs. The arrows indicate new positions of the maximum and minimum in the self-consistent Hartree approximation.

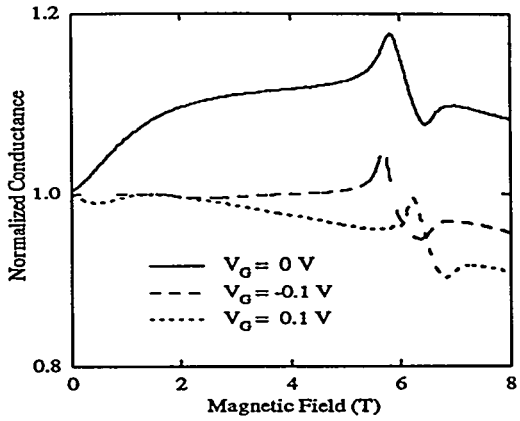

FIG. 7. In-plane conductance data from the DQW sample as a function of $B_{||}$. Charges are approximately balanced at the gate bias V_G = -0.1 V.

6 is then reduced to $175\times B_{||}/200$ as indicated by the thick arrows. In the absence of damping G vanishes at the minimum. The sharp minimum and maximum are rounded by the level damping as shown by the $\Gamma_0 > 0$ curves in Fig. 6. The theoretical result agrees reasonably well with our data shown in Fig. 7 [4].

The effect of damping is considered in the following linear response theory for G. The in-plane conductivity is given by

$$\sigma = \frac{e^2\hbar}{\pi\Omega}\sum_{\alpha k}(\mathbf{u}\cdot\mathbf{v}_{\alpha k})^2\int_{-\infty}^{\infty}[-f(z)']G_{\alpha k}(z-i0)G_{\alpha k}(z+i0)dz, \tag{6}$$

where $f(z)' \simeq \delta(z - \mu)$ is the first derivative of the Fermi function and Ω is the sample volume. The vertex correction can be neglected for isotropic scattering, relevant for short-range impurity potentials. The spin degeneracy is included in (2). The Green's function is defined by

$$G_{\alpha k}(z) = [z - \varepsilon_{\alpha k} - S_{\alpha k}(z)]^{-1}. \tag{7}$$

Here we employ a simple approximation for the self-energy part:

$$S_{\alpha k}(z) = U^2\sum_{\alpha' k'}G_{\alpha' k'}(z) \tag{8}$$

where U represents the scattering matrix. The real and imaginary parts of the self-energy then become independent of the subscripts α and $\mathbf{k}$:

$$S_{\alpha k}(z - i0) = M(z) + i\Gamma(z). \tag{9}$$

The DOS per area is given by

$$\rho(z)=\frac{1}{\pi A}\mathrm{Im}\,G(z-i0)=(\frac{m^*}{\pi\hbar^2})\Gamma(z)/\Gamma_o, \tag{10}$$

where $2\Gamma_o = Am^*U^2/\hbar^2$ is the field-free damping at the Fermi surface in the Born approximation with both branches populated and A is the area of the QW. For short-range scattering, the quantity Γ_o can be estimated from the mobility. The k_x-integration in (8) is performed, yielding self-consistent coupled equations for the real and imaginary parts of the self energy:

$$\left\{\frac{\Gamma(z)}{M(z)}\right\}=\pm\frac{\Gamma_o}{\pi}(0.196m_o/m^*)^{1/2}\int_{-\infty}^{\infty}\sum_{\alpha}\left(\frac{\sqrt{u_\alpha{}^2+\Gamma(z)^2}\pm u_\alpha}{u_\alpha{}^2+\Gamma(z)^2}\right)^{1/2} d(k_y\times 100\text{Å}). \tag{11}$$

Here $u_\alpha = z - \varepsilon(k_y) - M(z)$, the energy is in units of meV, and the square root vanishes for a negative argument. Eq. (11) is solved by an iterative method. The DOS is obtained from (10) and (11). The DOS is similar to those displayed in Figs. 2(b) and 3(b) except that sharp corners as well as the divergences are rounded, yielding the rounding effect for G [6]. Also, the energies are slightly lowered. A cutoff is introduced for the integrals in (11) to avoid a logarithmic divergence. The result is, however, insensitive to the cutoff. The latter is implicitly assumed in the **k'** summation in (8) because U vanishes for large k'. The conductance is obtained by inserting $\Gamma(z)$ and $M(z)$ in (6) and summing over **k** and is plotted in Fig. 6 as a function of $B_{||}$ for three values of Γ_o. It is seen that damping rounds the sharp $B_{||}$-dependent conductance structures, bringing the theoretical result closer to the data shown in Fig. 7. The minigap can be determined experimentally from the two values of $B_{||}$ where μ lies on the upper and lower gap edges [4]. Finally, our model predicts that in a low-density system (e.g., $N = 5\times10^{10}\ cm^{-2}$ in Fig. 5) with μ below the upper gap edge at $B_{||} = 0$, the $B_{||}$-dependent conductance has only a minimum, without the maximum peak arising from the depopulation of the upper branch. This interesting behavior has not been observed yet due to the difficulty of growing low-density high-mobility samples.

4. Cyclotron Mass

A small perpendicular magnetic field $B_\perp$ superimposed on an arbitrary parallel in-plane field $B_{||}$ induces Shubnikov-de Haas (S-dH) resistance oscillations δR which are much smaller than the total resistance R_0 at $B_\perp = 0$ [11]:

$$\frac{\delta R}{4R_0}=\sum_{s=1}^{\infty}\frac{X_s}{\sinh(X_s)}\exp(\frac{-s\pi}{\omega_c\tau})\cos(\frac{2\pi s\varepsilon_F}{\hbar\omega_c}-s\pi). \tag{12}$$

Here the right-hand side includes contributions from all orbits, $X_s = 2\pi^2 sk_BT/\hbar\omega_c$, $\omega_c = eB_\perp/m_c c$, and m_c is the cyclotron mass. The quantities ε_F, τ, and T are the Fermi energy, quantum scattering time, and temperature, respectively. The coefficient of the cosine factor in (12) is a monotonically decreasing function of m_c for arbitrary $B_\perp$ and T. This coeffi-

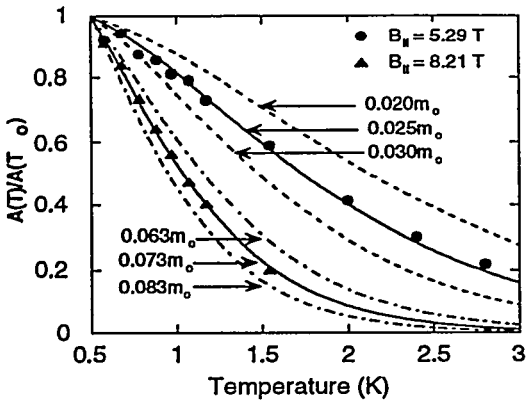

FIG. 8. Fit of SdH amplitude data to (13) for two $B_{\|}$ values and $T_0 = 0.5$ K.

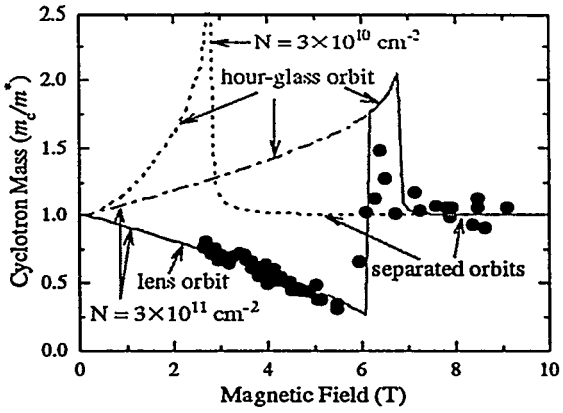

FIG. 9. Comparison of the reduced cyclotron mass data (black dots) with theory (solid curve) without adjustable parameters.

cient is dominated by the exponential factor. The main contribution to (12) arises from the fundamental component $s = 1$ for typical situations $\omega_c\tau \leqslant 1$ [6, 8]. The exponent is proportional to the cyclotron mass m_c. As will be shown later, m_c of the hour-glass orbit in Fig. 4 is much larger than m_c of the lens orbit, causing the former to yield a negligible contribution to the S-dH oscillations in (12): the electrons in the hour-glass orbit move slowly and are scattered before completing a cycle.

The $\delta R / 4R_0$ S-dH data show periodic oscillations in $1 / B_{\perp}$ [6, 8]. Both the observed period ($\propto 1 / m_c$) and the oscillation amplitudes change significantly as a function of $B_{\|}$, indicating that the measured cyclotron mass goes through drastic changes [6, 8]. For the fundamental component $s = 1$, the ratio of the amplitudes of the oscillations in (12) at temperatures T_0 and T are given by

$$\frac{A(T)}{A(T_o)} = \frac{T\sinh(X_1(T_o))}{T_o\sinh(X_1(T))}. \tag{13}$$

We plot this ratio in Fig. 8 as a function of T for several values of m_c and $T_0 = 0.5$ K and compare with the data from the same symmetric DQW sample at two $B_{\|}$ values [6, 8]. (Because the small $B_{\perp}$ was experimentally introduced by tilting the applied magnetic field 3° out of the sample's growth plane, $B_{\perp} = B_{\|}tan3°$ is different for the two $B_{\|}$ values.) The sensitive dependence of the curve on m_c and the degree of the fitting to the data indicate the high accuracy of the determination of the mass. The cyclotron mass so determined is plotted as black dots in Fig. 9 as a function of $B_{\|}$ [8].

The mass is given by $m_c = (\hbar^2/ 2\pi)\partial S/\partial\varepsilon$ where S is the area of the orbit in k-space and ε is the energy of the electron in the orbit on the Fermi surface [12, 13]. In 2D structures, this relationship can be rewritten as

$$m_c = m^*\rho(\varepsilon_F)/\rho_0, \tag{14}$$

where $\rho_0 = m^*A/(2\pi\hbar^2)$ is the well-known constant DOS per spin of a 2D parabolic energy dispersion. Spin splitting is neglected. The reduced mass m_c/m^* then equals the reduced DOS $\rho(\varepsilon_F)/\rho_0$. The reduced mass is calculated from (14) in the absence of damping by employing (3) and using the sample parameters d = 195 Å and $(\Delta z_1)^2$ = 1150 Å^2 determined by the self-consistent Hartree approximation, and E_g = 1.2 meV determined experimentally from the $B_{||}$ values of the maximum and minimum in G shown in Fig. 7 [4]. The contribution from the hour-glass orbit is neglected at low fields ($B_{||} < 6.1$ T), because S-dH oscillations from the lens orbit are expected to dominate whenever the hour-glass orbit is occupied. The result contains no adjustable parameters and yields excellent agreement with the data as shown in Fig. 9. The various orbits responsible for the measured m_c are indicated therein. The mass m_c from the sample's hour-glass orbit is shown in a dash-dotted curve at low fields (< 6.1 T) and is much larger than m_c from the inner lens orbit, as mentioned earlier. The abrupt increase of m_c at 6.1 T and sudden drop at 6.9 T occur when μ crosses the upper and lower gap edges, respectively. As discussed earlier, the conductance exhibits a maximum and a minimum at these fields. In a low-density system (e.g., $N = 3\times10^{10}cm^{-2}$), the $B_{||}$-dependent behavior of m_c is strikingly different from that of a high-density system, as shown by the dotted curve in Fig. 9. In this case, μ is below the upper gap edge and the electrons are in the hour-glass orbit at all low fields $B_{||}$ < 3 T. The mass m_c increases rapidly until μ passes through the saddle point at $B_{||} \simeq$ 3 T. The orbit splits into two separated orbits beyond this field and m_c drops abruptly, saturating at m^*.

A qualitative understanding of the $B_{||}$-dependent behavior of the measured m_c is gained from the reduced DOS at several characteristic $B_{||}$'s shown in Fig. 10. At zero field, the contribution to $\rho(\varepsilon)/\rho_0$ from the inner orbit in the upper branch equals unity as shown in Fig. 10(a), yielding m_c / m^* = 1. As $B_{||}$ is increased to $B_{||}$ = 5.8 T, μ sweeps through the shaded region toward the bottom of the upper branch in Fig. 10(a) and moves to a new position as shown in Fig. 10(b). At the same time, the energy dispersion as well as the DOS goes through a dramatic change; a saddle point with a large DOS

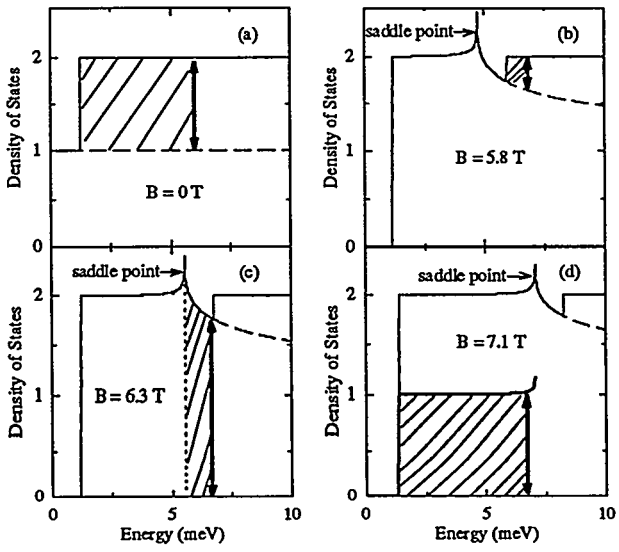

FIG. 10. Reduced DOS from the lower branch (dashed curve) and the upper branch (between the dashed and the solid curves) at several $B_{||}$'s. μ lies above, inside, and below the minigap in (a, b), (c), and (d), respectively. The double-arrowed thick bars at μ denote m_c/m^* and sweep through the shaded area with increasing $B_{||}$. In (d), the shaded part indicates half the DOS from the lower branch.

emerges in the lower branch, while the contribution to the DOS at μ from the upper branch continues to decrease as shown in Fig. 10(b). As a result, the contribution to $\rho(\varepsilon)/\rho_0$ from the upper branch decreases monotonically to $m_c / m^* = 0.26$ until $B_{||} = 6.1$ T as shown in Fig. 9. As $B_{||}$ rises above 6.1 T, the upper branch becomes empty and the electrons are in the hour-glass orbit. In this field range, the contribution to the S-dH oscillation comes from this large orbit. As a result, $\rho(\varepsilon)/\rho_0$ increases abruptly as shown in Fig. 10(c), leading to a sudden increase of m_c above 6.1 T in Fig. 9. As $B_{||}$ increases further, μ sweeps through the shaded region in Fig. 10(c) from the bottom of the upper branch to the lower-branch saddle point where the DOS is very large. The DOS as well as m_c increases monotonically as shown in Fig. 10(c) and Fig. 9, respectively. At $B_{||} = 6.9$ T, μ falls below the saddle point and the electrons are divided into two identical separated orbits. Each orbit contributes an equal amount of states to the DOS corresponding to half of the total DOS (in symmetric DQWs), as indicated by the shaded area in Fig. 10(d). The mass m_c decreases abruptly above 6.9 T and then saturates at unity in high fields. Sharp edges in Fig. 9 are rounded in the presence of damping [7]. Finally, we plot m_c/m^* from the hour-glass orbit in a dash-dotted curve in Fig. 9 for the sample (i.e., $N = 3\times10^{11}\ cm^{-2}$). This curve joins the solid curve in the region 6.1 T $< B_{||} <$ 6.9 T smoothly at $B_{||} = 6.1$ T. The sum of m_c/m^* from the lens orbit and the hour-glass orbit equals 2 approximately in the low field region $B_{||} <$ 6.1 T. This is consistent with the fact that the total $\rho(\varepsilon_F)/\rho_0 \simeq 2$ as shown by the solid curves in Figs. 10(a) and 10(b).

5. Conclusions

We have reviewed our recent theoretical and experimental work on 2DEGs in strongly coupled double quantum wells in the presence of an in-plane magnetic field. This system displays unusual electronic and transport properties arising from a partial minigap. The minigap is formed due to the anticrossing of the two QW dispersion curves displaced relative to each other in the transverse in-plane direction in k-space by $B_{||}$. Sweeping $B_{||}$ moves the minigap through the Fermi level, deforming the Fermi surface from a two-component surface (with a lens orbit inside an hour-glass orbit), to a single-component surface (with only an hour-glass orbit), and then finally back to a two-separated-orbit structure, as μ lies above, inside, and below the gap, respectively. We showed that the density of states develops a sharp van Hove singularity at the lower gap edge, while transport properties such as the in-plane conductance and the cyclotron mass show sharp $B_{||}$-dependent structures as μ passes through the gap edges. In a high-density system, we have shown both theoretically and experimentally that the in-plane conductance has a maximum and a minimum when μ lies at the upper and lower gap edges, respectively. The cyclotron mass exhibits giant distortions, increasing abruptly from a minimum value at the conductance-maximum $B_{||}$ and dropping rapidly from a maximum value at the conductance-minimum $B_{||}$. The conductance maximum and the abrupt increase of the mass are shown to arise from the depopulation of the upper branch, while the conductance minimum is due to the van Hove singularity of the saddle point at the lower gap edge. On the other hand, the abrupt drop of the mass at the saddle point was shown to arise from splitting of the orbits. In low-density systems with only the lower branch populated at all fields, our theory pre-

dicts strikingly different behaviors for the conductance as well as the cyclotron mass [3, 9]. In this case, the conductance has only a minimum [3], while the cyclotron mass has only a sharp maximum [9]. There has been no experimental confirmation of these last predictions due to the difficulty of growing low-density high-mobility samples. High in-plane magnetic fields were shown to turn off the effective 2D-2D tunneling of the 2DEGs.

Acknowledgments

This work was supported by the Office of Basic Energy Sciences, Division of Materials Sciences, U. S. DOE under Contract No. DE-AC04-94AL8500.

References

1. T. J. Gramila, J. P. Eisenstein, A. H. MacDonald, L. N. Pfeiffer, and K. W. West, Phys. Rev. Lett. **66**, 1793 (1990).
2. J. P. Eisenstein, L. N. Pfeiffer, and K. W. West, Phys. Rev. Lett. **69**, 3804 (1992).
3. S. K. Lyo, Phys. Rev. B **50**, 4965 (1994).
4. J. A. Simmons, S. K. Lyo, N. E. Harff, and J. F. Klem, Phys. Rev. Lett. **73**, 2256 (1994).
5. A. Kurobe, I. M. Castleton, E. H. Linfield, M. P. Grimshaw, K. M. Brown, D. A. Ritchie, M. Pepper, and G. A. C. Jones, Phys. Rev. B **50**, 4889 (1994).
6. N. E. Harff, J.A. Simmons, S. K. Lyo, J. E. Schirber, J. F. Klem, and S. M. Goodnick, in *The Physics of Semiconductors: Proceedings of the 22nd International Conference, Vancouver, 1994, VOL. 1, 831*, edited by D. J. Lockwood (World Scientific, Singapore, 1995).
7. S. K. Lyo, J. A. Simmons, and N. E. Harff, in *The Physics of Semiconductors: Proceedings of the 22nd International Conference, Vancouver, 1994, Vol. 1, 843*, edited by D. J. Lockwood (World Scientific, Singapore, 1995).
8. J. A. Simmons, N. E. Harff, and J. F. Klem, Phys. Rev. B **51**, 11156 (1995).
9. S. K. Lyo, Phys. Rev. B **51**, 11160 (1995).
10. For a review and references, see T. Ando, A. B. Fowler, and F. Stern, Rev. Mod. Phys. **54**, 437 (1982).
11. P. T. Coleridge, R. Stoner, and R. Fletcher, Phys. Rev. B **39**, 1120 (1989).
12. N. W. Ashcroft and N. D. Mermin, "Solid State Physics" (Holt, Rinehart and Winston, New York, 1976) p. 233.
13. L. Smrcka and T. Jungwirth, J. Phys. (Condens. Matter) **6**, 55 (1994).